Research Article

First Step of the Oxygen Reduction Reaction on Au(111): A Computational Study of O_2 Adsorption at the Electrified Metal/Water Interface

Alexandra M. Dudzinski,[†] Elias Diesen,[†] Hendrik H. Heenen, Vanessa J. Bukas,* and Karsten Reuter

Cite This: *ACS Catal.* 2023, 13, 12074−12081

Read Online

ACCESS | 📊 Metrics & More | 📖 Article Recommendations | 🔲 Supporting Information

ABSTRACT: Local field effects at the electrical double layer change the energies of reaction intermediates in heterogeneous electrocatalysis. The resulting dependence on (absolute) electrode potential can be pivotal to a catalyst's performance in acid or alkaline media. And yet, such local field effects are very difficult to describe theoretically and are often ignored. In this study, we focus on O_2 adsorption as the first step of the oxygen reduction reaction (ORR) on Au(111). Different physical effects of the local field are elucidated and compared by systematically improving the model of the double layer: from an applied saw-tooth potential in vacuum to an implicit solvent model, and explicitly modeled water *via ab initio* molecular

dynamics (AIMD). We find that all models predict a dominant dipole-field type interaction that significantly strengthens O_2 binding at increasingly reducing conditions. However, only an atomically resolved solvent model such as provided by AIMD can properly capture the additional stabilization due to explicit H-bonding from the water network. This contribution comes with the formation of a peroxo-like surface species and a more dramatic field response around the ORR onset. Our results overall demonstrate the importance of including local electric field effects in models of the electrochemical interface, while assessing the level of detail that is required to be accounted for.

KEYWORDS: electrocatalysis, oxygen reduction reaction, adsorption, gold, electrochemical interface, field effects, solvation, ab initio molecular dynamics, implicit solvation, umbrella sampling
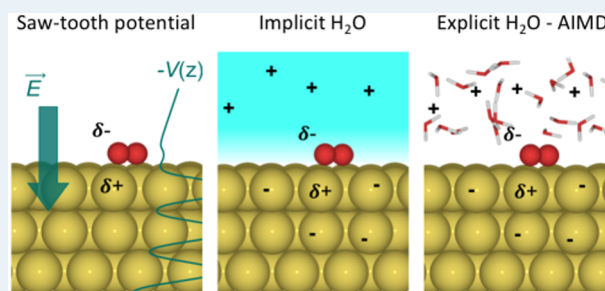
INTRODUCTION

First-principles simulations of electrochemical processes have contributed enormously to our current understanding of heterogeneous electrocatalysis. And yet, crucial methodological challenges remain. Electron transfer, ion effects, as well as structure and dynamics of the solvent are all very challenging to treat theoretically at the atomic level.[1−4] On top of all this, we are challenged with how to represent the constant electrode potential in first-principles simulations of the electrified metal/water interface.[5−12]

Simplified mechanistic models, commonly used in computational electrocatalysis, often rely on the inclusion of the applied electrode potential at the level of a thermodynamic electron reservoir. Charge-neutral reaction intermediates are computed from density functional theory (DFT) at conditions equivalent to the so-called potential of zero charge (PZC) and the effect of potential is then only included in a post-processing step as a simple shift to the PZC energetics. The latter is made possible by the computational hydrogen electrode (CHE) scheme which conveniently references the chemical potential of a transferred proton−electron pair to that of H_2 in the gas phase.[13] This elegant approximation thus allows to explore reaction thermodynamics without explicit treatment of

electrons and ions in solution. It further enables safe alignment to the experimental reversible hydrogen electrode (RHE) reference potential that includes both absolute potential, *e.g.*, against the standard hydrogen electrode (SHE), and proton activity.

Despite the appeal of treating charge-neutral intermediates in a periodic DFT simulation cell, the PZC calculations underlying the above methodology preclude any account of the potential-induced capacitive charging that characterizes the interface under realistic operating conditions. The resulting mechanistic assumption is that all electrochemical steps are viewed as proton-coupled-electron transfers (PCETs) that change only with the RHE potential scale, while any "chemical" steps of the reaction network are completely independent of potential. Here, the chemical step is meant to
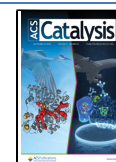
denote any elementary reaction step which does not include a Faradaic transfer of electrons such as, e.g., O_2 adsorption in the oxygen reduction reaction (ORR), CO_2 adsorption or CO dimerization in the electrochemical CO_2 reduction, etc. An improper description of such steps is of course particularly problematic if they happen to become rate determining. Indeed, while sufficient in many cases,[14] this simple charge-neutral picture is challenged by experiments showing electro-catalytic activity change with (absolute) potential or, equivalently, a pH dependence on the RHE scale for certain catalysts under certain conditions (cf. e.g., refs 15−18).

As an experimental signature, pH dependence on the RHE scale is characteristically found, e.g., during the ORR on weak binding electrode surfaces such as Au.[19−24] Competing pathways of a two-electron (toward H_2O_2) and four-electron (toward H_2O) reduction process as well as a strong facet-sensitivity paint a complicated picture for the ORR at Au electrodes. A recurring observation, however, is the superior catalytic performance in alkaline as compared to acidic media. Many have tried to explain this effect. For example, Ignaczak et al. suggested a faster reaction in base due to the formation of a stable superoxide ion that results from a first outer-sphere electron transfer.[25] Lu et al. suggested that surface-adsorbed H_2O acts as a proton donor and hence promotes the ORR in alkaline media.[26] On the other hand, Vassilev and Koper,[27] Duan and Henkelman,[28] and Kelly et al.[29] all argued as key the stabilization of adsorbed OOH* due to local field effects at the electrified metal/water interface. Despite these and many more studies, the identity of the rate-determining step and even the ability to bind O_2 as a first mechanistic step remains under debate. To the best of our knowledge, O_2 has only ever been detected in a physisorbed state above Au in ultra-high-vacuum,[30] but it is unclear how this situation may change in an electrochemical environment under reaction conditions. Such questions bring capacitive charging and the resulting local electric field effects into perspective.

In this study, we focus on O_2 adsorption as the first step of the ORR on Au(111). Going beyond the PZC/CHE methodology, we present results from three increasingly sophisticated models of the electric double layer: a vacuum background with applied saw-tooth potential, an implicit solvent model, and explicitly modeled aqueous solvent via ab initio molecular dynamics (AIMD). Systematically improving the description of the electrochemical interface elucidates field effects of different physical origins. We find all models agree in their description of dipole-field type interactions and predict significantly enhanced O_2 binding for potentials relevant to ORR operation. However, only an atomically resolved solvent model such as provided by AIMD properly captures the added contribution from explicit H-bonding interactions that mark the formation of a peroxo-like surface species around the ORR onset. Our results overall demonstrate the importance of including local electric field effects in models of the electrochemical interface, while assessing the level of detail that is required to be accounted for.

METHODS

All DFT calculations are performed using the VASP package[31−33] based on the projector-augmented wave (PAW) method[34,35] and a plane wave basis set in periodic boundary conditions. We employ the RPBE[36] exchange−correlation functional and D3 dispersion correction scheme,[37,38] as this setup has been reported to perform well for similar

systems.[39,40] Calculations including O_2 are spin-polarized. All simulations represent the Au(111) surface via a (non-symmetric) three-layer 3×4 supercell with the two bottom layers kept fixed, and a vacuum region of at least 14 Å separating the periodic images in the z-direction perpendicular to the surface. Further details on the DFT settings can be found in the Supporting Information (Section S1.1). The applied saw-tooth potential, implemented in VASP, results in a constant electric field across the simulation cell in the z-direction (Supporting Information, Section S1.2). Our implicit H_2O simulations use the polarizable continuum model implemented in VASPsol[41,42] with relative permittivity ϵ_r = 78.4 as in bulk water (Supporting Information, Section S1.3).

Our AIMD simulations use the same Au(111) surface slab model as those with a vacuum background, but add roughly "three" layers of interfacial water. This corresponds here to 24 explicit H_2O molecules. Following the setup by Heenen et al.,[43] we include a 7 Å vacuum region on either side of the slab and apply a dipole correction.[44] The NVT ensemble is sampled at 300 K using a Nosé−Hoover thermostat (damping coefficient 40 fs) and a timestep of 1 fs (Supporting Information, Section S1.4.1). We charge the interface by describing randomly selected H atoms of the H_2O solvent with parametrized PAW potentials (included in the standard VASP distribution) of 1.25 or 0.75 valency. The extra −0.25 or missing +0.25 electron charge (e), as well as multiples thereof, is added to or subtracted from the Au surface, depending upon whether we want to model reducing or oxidative conditions, respectively (Supporting Information, Section S1.4.2). For each total surface charge considered, we run several trajectories with and without O_2 (Table S1). Images representing chemisorbed O_2 are considered those with the molecule's center-of-mass distance from the surface <3 Å, as well as magnetic moment μ < 1 (μ_B units are implied here and throughout). Information on how we estimate the averages and errors for the AIMD-predicted adsorption energy at each value of surface charge can be found in the Supporting Information (Section S2). At this point, it should be noted that fully converged structures and energies require sampling times that are well beyond those currently feasible within AIMD. Our analysis shows locally converged behavior within 40 ps, however, similar to what has been reported previously.[43,45,46] Running a number of different trajectories (Table S1) then provides us with a more representative picture over the various local minimum water structures, along with a corresponding uncertainty analysis (Supporting Information, Section S2.2).

In calculating the electronic O_2 adsorption energy, we correct for the well-known oxygen over-binding predicted by semi-local DFT functionals[47] by assuming that all the error resides in the gaseous $O_2(g)$ reference. This error is then easily corrected by the difference between the experimental standard free energy of $H_2O(l)$ formation[48] and the theoretical value using our computational setup (Supporting Information, Section S3.1). The validity of this assumption is difficult to gauge and we note that absolute values of adsorption energies should be taken with some caution, also recognizing that our surface model does not consider the well-known "herringbone" reconstruction.[49] None of these uncertainties will strongly affect the relative field-induced energetics that is the primary focus of this study though.

Free energy contributions based on the ideal gas and harmonic approximations are added to the electronic adsorption energy E_{ads} (eq 2) in order to arrive at the

adsorption free energy G_{ads} plotted in Figure 1. These free energy contributions are calculated in a vacuum-background
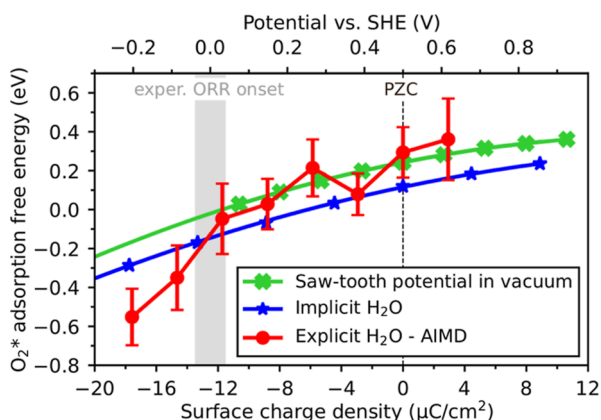

Figure 1. Free energy of O_2^* adsorption at Au(111) as a function of surface charge density (bottom x-axis) or applied potential vs SHE (top x-axis). Compared are different models of the electrical double layer as indicated in the figure's legend: a vacuum background with applied saw-tooth potential (green crosses), an implicit solvation model (blue stars), and explicitly modeled H_2O via AIMD simulations (red circles). The vertical dashed line and shaded gray area mark the PZC and (approximate) experimental onset of the ORR, respectively, see text.

simulation cell at conditions equivalent to the PZC and assumed the same for varying potential conditions (Supporting Information, Section S3.2). Static calculations consider zero-point-energy, enthalpy, and entropy contributions, while in the case of our AIMD simulations, we leave out the enthalpy contributions as these are already included via the sampling.[50]

Comparing the three double-layer models in this study requires that we convert between the (constant) interfacial field $\vec{E}$ introduced via the applied saw tooth potential, and the (effective) surface charge density σ controlled directly through excess charge in the implicit solvation or AIMD models. For this conversion, we assume that the double layer at the flat single-crystal surface behaves like a simple parallel-plate capacitor that can be related to the (absolute) electrode potential U_{SHE} according to

$$\vec{E} = \frac{\sigma}{\epsilon_r \epsilon_0}\hat{z} = \frac{C(U_{SHE} - U_{PZC})}{\epsilon_r \epsilon_0}\hat{z} \qquad (1)$$

where ϵ_0 is the vacuum permittivity ($=8.85 \times 10^{-12}$ F/m), and ϵ_r the dielectric constant of interfacial water which we set here to 1.5 as this is in line with values reported in the literature.[12,51] We further use the experimental $U_{PZC} = 0.5$ V for the PZC of Au(111)[52] and, for simplicity, a constant $C = 25$ μF/cm^2 value for the Helmholtz capacitance.[29,53−56] By referencing to U_{PZC}, eq 1 inherently assumes the same capacitance for the clean and oxygen-covered Au surfaces. This is a good approximation at sufficiently low O_2^* coverages, $i.e.$, approaching the infinitely dilute limit.[57] We stress, however, that the present approach should not be confused with so-called grand-canonical DFT simulations which give a more exact representation of reaction energies at a constant applied potential.[58]

Finally, free energy simulations are performed using umbrella sampling.[59] The O_2 center-of-mass distance from the surface is chosen as the collective variable, and sampling is

initiated from selected AIMD images to accelerate the required equilibration (Supporting Information, Section S4).

■ RESULTS AND DISCUSSION

We model O_2 adsorption at the electrochemical Au(111) interface by starting with the crudest approximation of the electrical double layer. In this approximation, we completely neglect the aqueous solvent and apply a sawtooth potential across the metal/vacuum interface to simulate the local potential drop driving the ORR. We relax the O_2 adsorbate at each applied field $\vec{E}$ and the lowest-energy configuration is used to predict the adsorption energy at that field as

$$E_{ads}(\vec{E}) = E_{O_2^*}(\vec{E}) - E_*(\vec{E}) - E_{O_2(g)} \qquad (2)$$

where $*$ and O_2^* denote the clean surface and surface-bound O_2 configurations, respectively. With this definition, more negative E_{ads} denote a stronger binding to the electrode. Correcting for the well-known over-binding in gaseous $O_2(g)$ predicted by semi-local DFT and adding free energy contributions to eq 2 (Methods and Supporting Information, Section S3) ultimately gives the free energy of O_2 adsorption $G_{ads}(\vec{E})$ as a function of the local electric field. We can also express this relation, however, in terms of capacitive charging through an (effective) surface charge density σ or (absolute) electrode potential U_{SHE} by assuming that the double layer behaves like a simple parallel-plate capacitor (Methods, eq 1). While such a picture holds a number of approximations that should be kept in mind, it allows us to draw a direct relation to experimental potential conditions as well as compare against different theoretical models of the double layer in the following. Results of G_{ads} as a function of σ (bottom x-axis) and U_{SHE} (top x-axis) are thus plotted in Figure 1 for a potential window relevant to ORR, between $ca.$ +1.0 and −0.3 V vs SHE.

In the absence of an electric field, $i.e.$, at conditions equivalent to the PZC ($\vec{E} = 0$, $\sigma = 0$, $U_{SHE} = U_{PZC}$), Figure 1 shows endothermic O_2 adsorption with $G_{ads} = +0.3$ eV in vacuum. We consider here only the lowest-energy chemisorbed state for which the magnetic moment is fully quenched ($\mu = 0$). This state features an atomic configuration where O_2^* lies parallel to the surface and with its center of mass above a bridge site, in agreement with previous studies.[27] While this configuration remains essentially unchanged with varying saw-tooth potential (Figure S7), O_2^* is considerably stabilized under electric fields that represent more reducing conditions. Stabilization within the present double-layer model is due to a purely electrostatic interaction. In terms of a dipole-field picture, the strength of this interaction can be measured by fitting to a (truncated) second-order polynomial

$$G_{ads}(\vec{E}) = G_{ads}^{PZC} + \vec{p}\vec{E} - \frac{\alpha}{2}\vec{E}^2 \qquad (3)$$

which yields here $p_z = 0.21$ $e\cdot$Å and $\alpha_{zz} = 0.15$ $e\cdot$Å^2/V for the z-components of the O_2^* intrinsic dipole moment and polarizability, respectively. As a result, at the more negative potentials in Figure 1, O_2 chemisorption is favored by a considerable $ca.$ 0.7 eV compared to PZC and predicted to be overall exothermic ($G_{ads} < 0$). Already this very crude model of the electrical double layer therefore captures a critical dependence on (absolute) potential that suggests O_2 adsorption as a first electrochemical, rather than purely chemical, step of the mechanism.

Refining the model to include solvation at the level of an implicit H_2O electrolyte does not add much to the above picture. In this approach, we explicitly charge the interface, while maintaining overall charge neutrality by following a Poisson−Boltzmann distribution of the corresponding counter-charge over the polarizable continuum that represents the solvent.[9,60,61] This allows for calculating E_{ads}, and as an extension G_{ads}, as a direct function of the excess surface charge σ. Figure 1 shows that this model yields, at least in this situation, the same qualitative G_{ads} curve as obtained from the vacuum simulations above. Implicit solvation can be thought of as providing a more physically inspired model of the electrical double layer but captures essentially the same physics in terms of the adsorbate's response to the applied field. Fitting to eq 3, we indeed find very similar values for the dipole moment and polarizability (Table S3). The only quantitative difference in G_{ads} is an almost constant *ca.* 0.1 eV stabilization which represents a slightly favorable interaction with the solvent and depends somewhat on the model parameters (Supporting Information, Section S1.3). As a technical side remark, however, we note that the implicit charging approach offers the advantage of a more stable electronic convergence at stronger fields. This advantage comes with an almost negligible added computational cost as compared to the vacuum simulations.

Our next and final model of the double layer is the most accurate, yet most computationally costly, as it explicitly includes the dynamical H_2O electrolyte with atomic resolution. *Ab initio* molecular dynamics simulations are performed within the *NVT* ensemble, sampling the O_2 and interfacial water structures at room temperature. In this approach, we charge the interface while supplying explicit counter-charge onto the core of randomly selected H atoms of the electrolyte. These charge-modified H atoms are mobile within the H_2O network and are not expected to influence the surface chemistry (Figures S2 and S3). We run several trajectories with and without O_2 for a specific surface charge density σ and the adsorption energy in each case is taken from the difference in ensemble averages while focusing only on chemisorbed O_2^* (Supporting Information, Section S2). Following a similar procedure from E_{ads} as above, finally gives G_{ads} as a function of σ. As depicted in Figure 1, the resulting AIMD data can be discussed in two potential regimes: closer to the PZC, G_{ads} shows remarkable quantitative agreement and even decreases with potential in a very similar way as in the much simpler vacuum and implicit H_2O models. Around 0 V *vs* SHE, however, the slope changes as G_{ads} drops abruptly below zero and becomes increasingly negative at more reducing conditions. The onset of this change, marked by gray in Figure 1, coincides with the (approximate) experimental onset of the ORR[19,21] (where the included uncertainty range is meant to capture some of the variation found between different studies in the experimental literature).

The explicit H_2O solvent adds to the double-layer model a full atomistic account of the dynamic interfacial H_2O network, including any adsorbate stabilization from directional H-bonding interactions. It is exactly this effect that gives rise to the stronger O_2^* binding in the more reducing potential regime of Figure 1. Analyzing our AIMD trajectories, we count an almost constant average of about two H-bonds to O_2^* in the high potential region around the PZC (where the definition of an H-bond follows that of ref 43). As shown in Figure 2a, however, this situation changes to a linearly increasing number
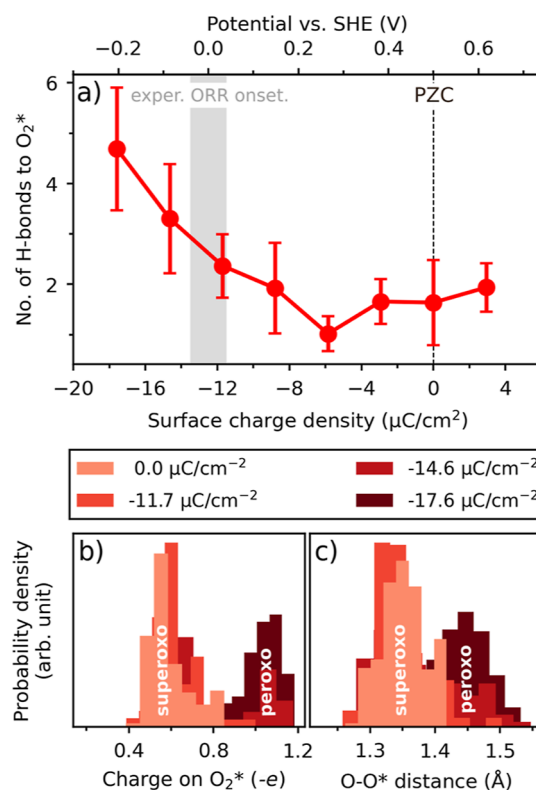

Figure 2. (a) Average number of H-bonds to O_2^* predicted from AIMD as a function of surface charge density (bottom x-axis) or applied potential *vs* SHE (top x-axis). The vertical dashed line and shaded gray area mark the PZC and (approximate) experimental onset of the ORR, respectively. (b) Probability density of the partial charge on O_2^* as estimated from Bader charge analysis for different values of surface charge density as listed in the figure's legend. The distribution distinguishes the superoxo- from the peroxo-like O_2^* dominating the surface at higher and lower potentials, respectively. (c) Same as panel (b), but for the intermolecular O−O* distance predicted from AIMD.

of H-bonds when further reducing to $U_{SHE} < 0$ V or, equivalently, $\sigma < -12$ $\mu C/cm^{-2}$. Stronger affinity towards H atoms of the H_2O solvent even leads to spontaneous OOH* formation during the AIMD, with increasing probability at more negative potentials, which requires that we sample a larger number of trajectories due to the practical challenge of stabilizing the (unprotonated) O_2^* adsorbate (Table S1). We determine the reason behind this change as a potential-dependent transition from a superoxo- to a peroxo-like O_2^* species at the surface. Between these two states, the peroxo species forms with increased charge transfer from the Au surface to the molecule's anti-bonding $2\pi^*$ orbitals and thus features a weakened O−O* bond (Figures S8 and S9). As a result, the superoxo and peroxo O_2^* are distinct from one another in terms of their natural charge state, magnetic moment, intramolecular bond length, and O−O* stretching frequency, as also previously discussed by, *e.g.*, Panchenko *et al.*[62] We indeed show in Figure 2b), *e.g.*, a bimodal distribution for the partial charge on chemisorbed O_2^*: a peak centered approximately around -0.6 e represents a dominant superoxo state near PZC ($\sigma > -12$ $\mu C/cm^{-2}$), while a second peak around -1.1 e represents a dominant peroxo state in the more negative potential regime ($\sigma < -12$ $\mu C/cm^{-2}$). A similar picture is seen for the intramolecular O−O* bond length in

Figure 2c) with peaks around 1.33 and 1.44 Å for the superoxo and peroxo species, respectively. These values are in line with the definition of the two chemisorbed O_2^* states by Montemore et al.[30] We note that the peroxo-like O_2^* could be viewed as a PCET precursor state given its spontaneous protonation to OOH* (or even, less occasionally, H_2O_2) during our AIMD. Such classification is, however, ambiguous on the basis of our simulations and involves, at least to some degree, a semantic discussion to differentiate.

All available states in competition for adsorbing O_2 under varying potential conditions can be found in the underlying free energy landscape. For this purpose, we perform umbrella sampling simulations for different values of σ in a setup similar to that used for the AIMD. Figure 3 plots the resulting free energy profile as a function of the O_2 center-of-mass distance from the surface at increasingly reducing conditions (from top to bottom, panels a−c). At the PZC ($\sigma = 0$), Figure 3a shows a dominant physisorption well around 3.2 Å above the surface that has O_2 residing in the first interfacial H_2O layer. Approximate boundaries for this H_2O layer are marked by
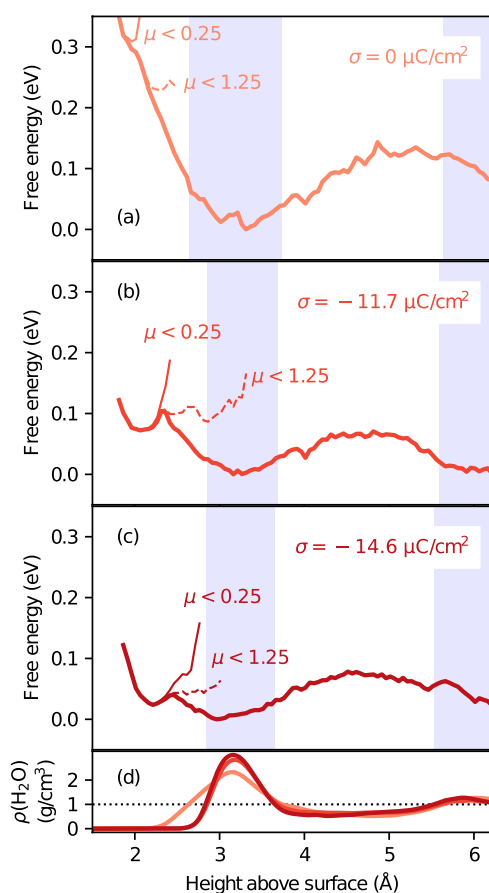

Figure 3. (a−c) Free energy profiles as a function of O_2 center-of-mass distance above the surface predicted from umbrella sampling simulations for increasingly negative values of surface charge density, i.e., increasingly reducing conditions. Resolving the full statistics of the free energy (thick solid line) with respect to the magnetic moment reveals the chemisorption minima assigned to the peroxo-like (thin line, $\mu < 0.25$) and superoxo-like O_2^* (dashed line, $\mu < 1.25$) states. The shaded blue areas mark the approximate boundaries of the first and second interfacial solvent layers according to the H_2O density profiles plotted in panel (d). The dotted line in panel (d) indicates the bulk H_2O density.

the shaded blue region according to the H_2O density profile in the lowermost panel, Figure 3d (detailed analysis in Figure S3). In line with this assignment, we find the shallow physisorption minimum features a weakly bound O_2 in its triplet spin state ($\mu = 2$). As such, this state is not included in the analysis underlying Figures 1 and 2 (which consider only chemisorbed O_2^*). Resolving the free energy surface with respect to magnetic moment, however, reveals the higher-energy (metastable) O_2^* states that give rise to the endothermic chemisorption predicted at the PZC in Figure 1. We specifically resolve two surface-bound states with partially or fully quenched spin, both of which lie between the surface and first H_2O layer: the well-defined minimum closest to the surface (at ca. 2.0 Å) is assigned to the peroxo-like O_2^* species (in line with the AIMD analysis, Figure S9). This state is characterized by an essentially negligible spin (outlined in Figure 3 as $\mu < 0.25$) and an atomic configuration that is consistent with that found in vacuum, i.e., where O_2^* lies parallel to the surface and with its center-of-mass above the bridge (Figure S10). Further away from the surface, the superoxo-like O_2^* state is not as easily defined as it is represented by a flatter region of the free energy landscape and a rather wide range of possible spin values (in agreement with ref 30). While outlined in Figure 3 as $\mu < 1.25$, we note that choosing a slightly lower or higher cut-off of μ in defining this state simply shifts its relative population in what we consider here as chemisorbed (resulting in a slightly different adsorption free energy) and does not change the qualitative results (cf. sensitivity analysis in Figure S6). In any case, between the two chemisorbed O_2^* states, the lower free energy of the superoxo state rationalizes its preference over the peroxo state around the PZC, as seen in the AIMD.

The PZC free energy landscape changes with increasingly reducing conditions. Figure 3b specifically shows two changes in relative stability: first, the two chemisorption states are both energetically shifted towards the physisorption minimum. This shift explains the initial decrease of G_{ads} in Figure 1 (as well as the larger fraction of chemisorbed AIMD images at more negative potentials, Table S1). Simultaneously, both chem-isorbed O_2^* configurations move away from the surface as the first interfacial H_2O layer becomes more compact (again, in line with the AIMD analysis, Figures S3 and S9). Second, the peroxo state is stabilized against the superoxo O_2^* state. This effect is even more pronounced at increasingly negative σ with Figure 3c finally showing a preference for the peroxo over the superoxo O_2^*. We emphasize here again that only the inclusion of explicit adsorbate−solvent interactions can resolve the competition between these two states in our most sophisticated model of the electrical double layer. This explains the steeper decrease of G_{ads} at $\sigma < -12 \ \mu C/cm^2$ in Figure 1 via a growing peroxo population at the surface. We predict that this preference marks the transition to operating ORR potentials.

■ CONCLUSIONS

In summary, we show that O_2 adsorption depends strongly on the applied (absolute) potential through local electric field effects during the ORR on Au(111). This dependence suggests O_2 adsorption as a first electrochemical, rather than purely chemical step of the mechanism. We specifically predict that chemisorption is endothermic at the PZC, but becomes thermodynamically favorable around the experimental onset of the ORR at 0 V vs SHE. This result makes it easy to imagine

O_2 adsorption as the actual rate-determining step and explains why the overpotential for this process (measured on an RHE potential scale) depends on pH. Converting the onset of the reaction from SHE to an RHE scale yields, *e.g.*, 0.06 V *vs* RHE at pH = 1 and 0.77 V *vs* RHE at pH = 13. As discussed by others before,[16,24,25,29] these values are to be considered in relation to an equilibrium reaction potential. Here the equilibrium potential of 0.70 V *vs* RHE[63] for the two-electron ORR that dominates at the Au(111) electrode surface[20] translates into a significantly higher overpotential in acid as compared to alkaline media. This effect is entirely missed if assuming no potential dependence for O_2 adsorption within the PZC/CHE methodology, thus highlighting that electric field effects cannot be neglected in corresponding DFT models.

In predicting the system's response to applied potential, we find two effects of the local electric field that jointly contribute towards O_2^* stabilization. A dipole-field type interaction dominates around the PZC and is similarly captured by the simplest of our double-layer models, namely an applied saw-tooth potential in vacuum and an implicit aqueous solvent. Already this electrostatic effect is sufficient to recover a large part of the O_2^* stabilization with reducing potentials due to the adsorbate's considerable dipole moment. However, only an atomistic solvent model as provided by AIMD can capture the additional stabilization due to directional H-bonding from the H_2O network. We show that this effect sets in around the experimental onset of the ORR and attribute its origin to the concomitant preference for a peroxo-like O_2^* species at the surface. This state likely acts as a precursor to protonation, as evidenced by spontaneous OOH* formation in our AIMD, thus setting the stage for the next step of the ORR mechanism.

ASSOCIATED CONTENT

Ⓢ Supporting Information

The Supporting Information is available free of charge at https://pubs.acs.org/doi/10.1021/acscatal.3c02129.

> Computational and methodological details; AIMD trajectory analysis; corrections & free energy contributions; umbrella sampling; analysis of O_2 adsorption at the electrified interface; additional references (PDF)

AUTHOR INFORMATION

Corresponding Author

Vanessa J. Bukas — *Fritz-Haber-Institut der Max-Planck-Gesellschaft, D-14195 Berlin, Germany;* Ⓞ orcid.org/0000-0002-0105-863X; Email: bukas@fhi.mpg.de

Authors

Alexandra M. Dudzinski — *Fritz-Haber-Institut der Max-Planck-Gesellschaft, D-14195 Berlin, Germany;* Ⓞ orcid.org/0000-0003-4688-4369

Elias Diesen — *Fritz-Haber-Institut der Max-Planck-Gesellschaft, D-14195 Berlin, Germany;* Ⓞ orcid.org/0000-0002-8235-3920

Hendrik H. Heenen — *Fritz-Haber-Institut der Max-Planck-Gesellschaft, D-14195 Berlin, Germany;* Ⓞ orcid.org/0000-0003-0696-8445

Karsten Reuter — *Fritz-Haber-Institut der Max-Planck-Gesellschaft, D-14195 Berlin, Germany;* Ⓞ orcid.org/0000-0001-8473-8659

Complete contact information is available at:

https://pubs.acs.org/10.1021/acscatal.3c02129

Author Contributions

[†]A.M.D. and E.D. contributed equally to this work.

REFERENCES

(1) Warburton, R. E.; Soudackov, A. V.; Hammes-Schiffer, S. Theoretical Modeling of Electrochemical Proton-Coupled Electron Transfer. *Chem. Rev.* **2022**, *122*, 10599−10650.

(2) Santos, E.; Schmickler, W. Models of Electron Transfer at Different Electrode Materials. *Chem. Rev.* **2022**, *122*, 10581−10598.

(3) Ringe, S. Cation effects on electrocatalytic reduction processes at the example of the hydrogen evolution reaction. *Curr. Opin. Electrochem.* **2023**, *39*, 101268.

(4) Groß, A. Challenges for ab initio molecular dynamics simulations of electrochemical interfaces. *Curr. Opin. Electrochem.* **2023**, *40*, 101345.

(5) Letchworth-Weaver, K.; Arias, T. A. Joint density functional theory of the electrode-electrolyte interface: Application to fixed electrode potentials, interfacial capacitances, and potentials of zero charge. *Phys. Rev. B: Condens. Matter Mater. Phys.* **2012**, *86*, 075140.

(6) Chan, K.; Nørskov, J. K. Electrochemical Barriers Made Simple. *J. Phys. Chem. Lett.* **2015**, *6*, 2663−2668.

(7) Haruyama, J.; Ikeshoji, T.; Otani, M. Electrode potential from density functional theory calculations combined with implicit solvation theory. *Phys. Rev. Mater.* **2018**, *2*, 095801.

(8) Kastlunger, G.; Lindgren, P.; Peterson, A. A. Controlled-Potential Simulation of Elementary Electrochemical Reactions: Proton Discharge on Metal Surfaces. *J. Phys. Chem. C* **2018**, *122*, 12771−12781.

(9) Hörmann, N. G.; Andreussi, O.; Marzari, N. Grand canonical simulations of electrochemical interfaces in implicit solvation models. *J. Chem. Phys.* **2019**, *150*, 041730.

(10) Hörmann, N. G.; Marzari, N.; Reuter, K. Electrosorption at metal surfaces from first principles. *npj Comput. Mater.* **2020**, *6*, 136.

(11) Kristoffersen, H. H.; Chan, K. Towards constant potential modeling of CO-CO coupling at liquid water-Cu(100) interfaces. *J. Catal.* **2021**, *396*, 251−260.

(12) Deißenbeck, F.; Freysoldt, C.; Todorova, M.; Neugebauer, J.; Wippermann, S. Dielectric Properties of Nanoconfined Water: A Canonical Thermopotentiostat Approach. *Phys. Rev. Lett.* **2021**, *126*, 136803.

(13) Nørskov, J. K.; Rossmeisl, J.; Logadottir, A.; Lindqvist, L.; Kitchin, J. R.; Bligaard, T.; Jónsson, H. Origin of the Overpotential for Oxygen Reduction at a Fuel-Cell Cathode. *J. Phys. Chem. B* **2004**, *108*, 17886−17892.

(14) Seh, Z. W.; Kibsgaard, J.; Dickens, C. F.; Chorkendorff, I.; Nørskov, J. K.; Jaramillo, T. F. Combining theory and experiment in electrocatalysis: Insights into materials design. *Science* **2017**, *355*, 146.

(15) Hori, Y. Electrochemical CO_2 Reduction on Metal Electrodes. In *Modern Aspects of Electrochemistry 42*; Vayenas, C. G., White, R. E., Gamboa-Aldeco, M. E., Eds.; Springer: New York, 2008; pp 89−189.

(16) Koper, M. T. M. Theory of multiple proton−electron transfer reactions and its implications for electrocatalysis. *Chem. Sci.* **2013**, *4*, 2710−2723.

(17) Bukas, V. J.; Kim, H. W.; Sengpiel, R.; Knudsen, K.; Voss, J.; McCloskey, B. D.; Luntz, A. C. Combining Experiment and Theory To Unravel the Mechanism of Two-Electron Oxygen Reduction at a Selective and Active Co-catalyst. *ACS Catal.* **2018**, *8*, 11940−11951.

(18) Nitopi, S.; Bertheussen, E.; Scott, S. B.; Liu, X.; Engstfeld, A. K.; Horch, S.; Seger, B.; Stephens, I. E. L.; Chan, K.; Hahn, C.; Nørskov, J. K.; Jaramillo, T. F.; Chorkendorff, I. Progress and Perspectives of Electrochemical CO_2 Reduction on Copper in Aqueous Electrolyte. *Chem. Rev.* **2019**, *119*, 7610−7672.

(19) Marković, N. M.; Adžić, R.; Vešović, V. Structural effects in electrocatalysis: Oxygen reduction on the gold single crystal electrodes with (110) and (111) orientations. *J. Electroanal. Chem. Interfacial Electrochem.* **1984**, *165*, 121−133.

(20) Adžić, R.; Štrbac, S.; Anastasijević, N. Electrocatalysis of oxygen on single crystal gold electrodes. *Mater. Chem. Phys.* **1989**, *22*, 349−375.

(21) Štrbac, S.; Anastasijević, N.; Adžić, R. Oxygen reduction on Au(111) and vicinal Au(332) faces: A rotating disc and disc-ring study. *Electrochim. Acta* **1994**, *39*, 983−990.

(22) Štrbac, S.; Adžić, R. The influence of pH on reaction pathways for O_2 reduction on the Au(100) face. *Electrochim. Acta* **1996**, *41*, 2903−2908.

(23) Blizanac, B. B.; Lucas, C. A.; Gallagher, M. E.; Arenz, M.; Ross, P. N.; Marković, N. M. Anion Adsorption, CO Oxidation, and Oxygen Reduction Reaction on a Au(100) Surface: The pH Effect. *J. Phys. Chem. B* **2004**, *108*, 625−634.

(24) Rodriguez, P.; Koper, M. T. M. Electrocatalysis on gold. *Phys. Chem. Chem. Phys.* **2014**, *16*, 13583−13594.

(25) Ignaczak, A.; Nazmutdinov, R.; Goduljan, A.; de Campos Pinto, L. M.; Juarez, F.; Quaino, P.; Belletti, G.; Santos, E.; Schmickler, W. Oxygen Reduction in Alkaline Media—a Discussion. *Electrocatalysis* **2017**, *8*, 554−564.

(26) Lu, F.; Zhang, Y.; Liu, S.; Lu, D.; Su, D.; Liu, M.; Zhang, Y.; Liu, P.; Wang, J. X.; Adžić, R. R.; Gang, O. Surface Proton Transfer Promotes Four-Electron Oxygen Reduction on Gold Nanocrystal Surfaces in Alkaline Solution. *J. Am. Chem. Soc.* **2017**, *139*, 7310−7317.

(27) Vassilev, P.; Koper, M. T. M. Electrochemical Reduction of Oxygen on Gold Surfaces: A Density Functional Theory Study of Intermediates and Reaction Paths. *J. Phys. Chem. C* **2007**, *111*, 2607−2613.

(28) Duan, Z.; Henkelman, G. Theoretical Resolution of the Exceptional Oxygen Reduction Activity of Au(100) in Alkaline Media. *ACS Catal.* **2019**, *9*, 5567−5573.

(29) Kelly, S. R.; Kirk, C.; Chan, K.; Nørskov, J. K. Electric Field Effects in Oxygen Reduction Kinetics: Rationalizing pH Dependence at the Pt(111), Au(111), and Au(100) Electrodes. *J. Phys. Chem. C* **2020**, *124*, 14581−14591.

(30) Montemore, M. M.; van Spronsen, M. A.; Madix, R. J.; Friend, C. M. O_2 Activation by Metal Surfaces: Implications for Bonding and Reactivity on Heterogeneous Catalysts. *Chem. Rev.* **2018**, *118*, 2816−2862.

(31) Kresse, G.; Hafner, J. Ab initio molecular dynamics for liquid metals. *Phys. Rev. B: Condens. Matter Mater. Phys.* **1993**, *47*, 558−561.

(32) Kresse, G.; Furthmüller, J. Efficiency of ab-initio total energy calculations for metals and semiconductors using a plane-wave basis set. *Comput. Mater. Sci.* **1996**, *6*, 15−50.

(33) Kresse, G.; Furthmüller, J. Efficient iterative schemes for ab initio total-energy calculations using a plane-wave basis set. *Phys. Rev. B: Condens. Matter Mater. Phys.* **1996**, *54*, 11169−11186.

(34) Blöchl, P. E. Projector augmented-wave method. *Phys. Rev. B: Condens. Matter Mater. Phys.* **1994**, *50*, 17953−17979.

(35) Kresse, G.; Joubert, D. From ultrasoft pseudopotentials to the projector augmented-wave method. *Phys. Rev. B: Condens. Matter Mater. Phys.* **1999**, *59*, 1758−1775.

(36) Hammer, B.; Hansen, L. B.; Nørskov, J. K. Improved adsorption energetics within density-functional theory using revised Perdew-Burke-Ernzerhof functionals. *Phys. Rev. B: Condens. Matter Mater. Phys.* **1999**, *59*, 7413−7421.

(37) Grimme, S.; Antony, J.; Ehrlich, S.; Krieg, H. A consistent and accurate ab initio parametrization of density functional dispersion correction (DFT-D) for the 94 elements H-Pu. *J. Chem. Phys.* **2010**, *132*, 154104.

(38) Grimme, S. Density functional theory with London dispersion corrections. *Wiley Interdiscip. Rev.: Comput. Mol. Sci.* **2011**, *1*, 211−228.

(39) Sakong, S.; Groß, A. The electric double layer at metal-water interfaces revisited based on a charge polarization scheme. *J. Chem. Phys.* **2018**, *149*, 084705.

(40) Morawietz, T.; Singraber, A.; Dellago, C.; Behler, J. How van der Waals interactions determine the unique properties of water. *Proc. Natl. Acad. Sci. U.S.A.* **2016**, *113*, 8368−8373.

(41) Mathew, K.; Sundararaman, R.; Letchworth-Weaver, K.; Arias, T. A.; Hennig, R. G. Implicit solvation model for density-functional study of nanocrystal surfaces and reaction pathways. *J. Chem. Phys.* **2014**, *140*, 084106.

(42) Mathew, K.; Kolluru, V. S. C.; Mula, S.; Steinmann, S. N.; Hennig, R. G. Implicit self-consistent electrolyte model in plane-wave density-functional theory. *J. Chem. Phys.* **2019**, *151*, 234101.

(43) Heenen, H. H.; Gauthier, J. A.; Kristoffersen, H. H.; Ludwig, T.; Chan, K. Solvation at metal/water interfaces: An ab initio molecular dynamics benchmark of common computational approaches. *J. Chem. Phys.* **2020**, *152*, 144703.

(44) Bengtsson, L. Dipole correction for surface supercell calculations. *Phys. Rev. B: Condens. Matter Mater. Phys.* **1999**, *59*, 12301−12304.

(45) Sakong, S.; Forster-Tonigold, K.; Groß, A. The structure of water at a Pt(111) electrode and the potential of zero charge studied from first principles. *J. Chem. Phys.* **2016**, *144*, 194701.

(46) Groß, A.; Sakong, S. Ab Initio Simulations of Water/Metal Interfaces. *Chem. Rev.* **2022**, *122*, 10746−10776.

(47) Carbogno, C.; Groß, A.; Meyer, J.; Reuter, K. In *Dynamics of Gas-Surface Interactions: Atomic-level Understanding of Scattering Processes at Surfaces*; Díez Muiño, R., Busnengo, H. F., Eds.; Springer Berlin Heidelberg: Berlin, Heidelberg, 2013; pp 389−419.

(48) Dean, J. A., Ed. *Lange's Handbook of Chemistry*, 15th ed.; McGraw-Hill: New York, 1999.

(49) Min, B. K.; Deng, X.; Pinnaduwage, D.; Schalek, R.; Friend, C. M. Oxygen-induced restructuring with release of gold atoms from Au(111). *Phys. Rev. B: Condens. Matter Mater. Phys.* **2005**, *72*, 121410.

(50) Vijay, S.; Hogg, T. V.; Ehlers, J.; Kristoffersen, H. H.; Katayama, Y.; Shao Horn, Y.; Chorkendorff, I.; Chan, K.; Seger, B. Interaction of CO with Gold in an Electrochemical Environment. *J. Phys. Chem. C* **2021**, *125*, 17684−17689.

(51) Fumagalli, L.; Esfandiar, A.; Fabregas, R.; Hu, S.; Ares, P.; Janardanan, A.; Yang, Q.; Radha, B.; Taniguchi, T.; Watanabe, K.; Gomila, G.; Novoselov, K.; Geim, A. Anomalously low dielectric constant of confined water. *Science* **2018**, *360*, 1339−1342.

(52) Trasatti, S.; Lust, E. The Potential of Zero Charge. In *Modern Aspects of Electrochemistry 33*; White, R. E., Bockris, J. O'M., Conway, B. E., Eds.; Springer: New York, 1999; pp 1−215.

(53) Kofman, R.; Garrigos, R.; Cheyssac, P. Optical response of a charged metal-aqueous electrolyte interphase. *Thin Solid Films* **1981**, *82*, 73−80.

(54) Kolb, D.; Schneider, J. Surface reconstruction in electrochemistry: Au(100)-(5 × 20), Au(111)-(1 × 23) and Au(110)-(1 × 2). *Electrochim. Acta* **1986**, *31*, 929−936.

(55) Ojha, K.; Arulmozhi, N.; Aranzales, D.; Koper, M. T. M. Double Layer at the Pt(111)−Aqueous Electrolyte Interface: Potential of Zero Charge and Anomalous Gouy−Chapman Screening. *Angew. Chem., Int. Ed.* **2020**, *59*, 711−715.

(56) Bohnen, K.; Kolb, D. Charge-versus adsorbate-induced lifting of the Au (100)-(hex) reconstruction in an electrochemical environment. *Surf. Sci.* **1998**, *407*, L629−L632.

(57) Rossmeisl, J.; Skúlason, E.; Björketun, M. E.; Tripkovic, V.; Nørskov, J. K. Modeling the electrified solid−liquid interface. *Chem. Phys. Lett.* **2008**, *466*, 68−71.

(58) Domínguez-Flores, F.; Melander, M. M. Approximating constant potential DFT with canonical DFT and electrostatic corrections. *J. Chem. Phys.* **2023**, *158*, 144701.

(59) Torrie, G.; Valleau, J. Nonphysical sampling distributions in Monte Carlo free-energy estimation: Umbrella sampling. *J. Comput. Phys.* **1977**, *23*, 187−199.

(60) Gauthier, J. A.; Ringe, S.; Dickens, C. F.; Garza, A. J.; Bell, A. T.; Head-Gordon, M.; Nørskov, J. K.; Chan, K. Challenges in Modeling Electrochemical Reaction Energetics with Polarizable Continuum Models. *ACS Catal.* **2019**, *9*, 920−931.

(61) Ringe, S.; Hörmann, N. G.; Oberhofer, H.; Reuter, K. Implicit Solvation Methods for Catalysis at Electrified Interfaces. *Chem. Rev.* **2022**, *122*, 10777−10820.

(62) Panchenko, A.; Koper, M. T. M.; Shubina, T. E.; Mitchell, S. J.; Roduner, E. Ab Initio Calculations of Intermediates of Oxygen Reduction on Low-Index Platinum Surfaces. *J. Electrochem. Soc.* **2004**, *151*, A2016.

(63) Hoare, J. P. Oxygen. In *Standard Potentials in Aqueous Solution*; Bard, A. J., Parsons, R., Jordan, J., Eds.; Marcel Dekker, 1985; p 56.